UNIVERSITY OF CALIFORNIA

Los Angeles

A Non-Reciprocal Component with Distributedly Modulated Capacitors

A thesis submitted in partial satisfaction

of the requirements for the degree

Master of Science in Electrical Engineering

by

Shihan Qin

2013

ABSTRACT OF THE THESIS

A Non-Reciprocal Component with Distributedly Modulated Capacitors

by

Shihan Qin

Master of Science in Electrical Engineering

University of California, Los Angeles, 2013

Professor Yuanxun Ethan Wang, Chair

The requirement of using ferrite magnetic material for non-reciprocal microwave components like circulators and isolators prevents the designs from being small, lossless and broadband especially at the lower end of the microwave frequency spectrum. Active non-reciprocal components may have good isolation and can be integrated, but they are very poor in noise performance. A circuit with distributedly modulated capacitors (DMC) - time-varying capacitors distributed along a transmission line and modulated by a carrier wave - provides a novel realization of lossless and broadband non-reciprocity. The circuit is compatible with modern integrated circuit technology. Decent gain and low noise for receiving path are also possible as bonus advantages. Studies on the estimations of the isolation and the receiving insertion performance of the DMC circuit are focused in this thesis to show its ability to serve for a non-reciprocal component. A prototype made on Rogers circuit board has verified the theory's prediction on the performance, which is capable of achieving > 13 dB isolation between the transmitting and the receiving paths and < 5 dB receiving insertion loss over the frequency range of 0.5 – 1.8 GHz.

The thesis of Shihan Qin is approved.

Tatsuo Itoh

Yahya Rahmat-Samii

Yuanxun Ethan Wang, Committee Chair

University of California, Los Angeles

2013

Table of Contents

List of Figures

List of Tables

ACKNOWLEDGMENTS

I would like to thank my advisor, Professor Yuanxun Ethan Wang, for his guidance and support throughout this thesis. Without his knowledge and time, this research work would not have been possible. I am also grateful to Dr. Qiang Xu, who have many helpful discussions with me on this subject. In addition, I would like to express my gratitude to Dr. Minji Zhu for his instruction and help in the circuit fabrication. I also thank Professor Tatsuo Itoh and Professor Yahya Rahmat-Samii for their kindness of reviewing this thesis. It is a great honor for me to have them serve as my thesis committee. Finally, I would like to thank my parents and my friends in my home country who have been encouraging me till the day this work exists.

CHAPTER 1

Introduction

What is a non-reciprocal component? Why do we need it? Before introducing all the theories and designs recorded in this thesis, I think those questions are the very first to answer. However, instead of giving a general answer which may be beyond the focus of this thesis, I'd like to start with the specific problem that I have been trying to approach.

1.1 A Circulator as a Non-Reciprocal Component

With success of modern integrated circuit technology, there are continuing ambitions and needs of making everything small in this world. Many challenges remain including in designs of small electronic devices, as the tradeoff between size and performance is of great concern. In a wireless communication system, the antenna is still hard to integrate. As a result, it is a common practice for a transceiver, capable of both signal transmission and reception, to share a same antenna for the two functions in order to save the space, as realized in many cell phones.

Figure 1.1 shows a typical transceiver front-end with a device called duplexer in the

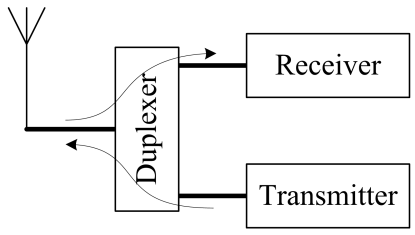

Figure 1.1: The duplexer in a transceiver front-end.

center connecting the antenna, the transmitter and the receiver. The duplexer is necessary to perform combination or separation of signal transmission and reception paths. In practice, it helps protect the receiver and makes independent transmitter and receiver designs possible under the single-antenna condition.

The duplexer can be in many forms, such as a switch or a frequency-diplexer (made of filters). The former does not give way to the application where transmission and reception at the same time, as in cell phone communication, is required, while the latter does not allow the same-frequency application for radar communication, for instance. If both simultaneity and the same-frequency constrain are required, a kind of duplexer called circulator can be used.

A circulator is known as a non-reciprocal component, as the signal flow in the forward direction is different from that in the reverse. A conceptual, three-port circulator shown in Figure 1.2a has ideally no mismatch in all ports, lossless insertion in the forward paths (namely, from port 1 to 2, port 2 to 3 and port 3 to 1) and no insertion in the reverse. The circulator in Figure 1.2a forms a clockwise circulation of the signal flow in three ports, but it is trivial to mention that counterclockwise circulators and those with more than three ports are also available.

When a circulator is connected as a duplexer shown in Figure 1.2b, some practical issues arise and there is much about what performances a good circulator should have. One of

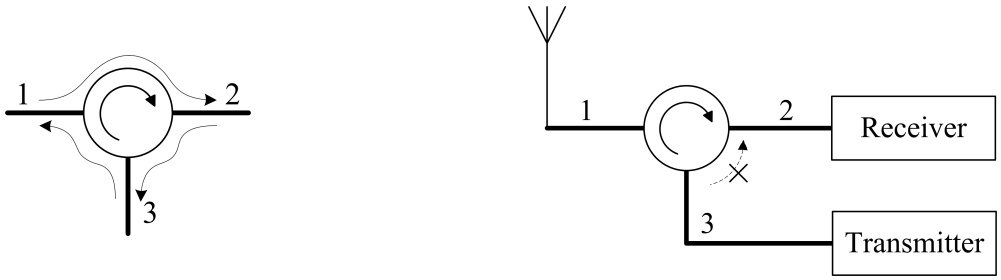

(a) (b)

Figure 1.2: (a) A three-port circulator. (b) A circulator in a transceiver front-end.

the concerns is that the leakage in the reverse path is inevitable, but in particular, the leaked signal from the transmitter (TX) to the receiver (RX), e.g. from port 3 to 2 in Figure 1.2b, need be as small as possible to protect the receiver from being jammed by the transmitter. It is referred as the TX/RX isolation performance of a circulator, and high isolation, corresponding to small leakage from TX to RX, is always desired. Another evaluation need be made on the noise performance of the receiving path, e.g. from port 1 to 2 in Figure 1.2b. Signals from the antenna to the receiver should gain little additional noise through the circulator so that they could be detected properly. Noise figure can be defined for the receiving path, and low noise figure is desired. Other concerns may include the physical size of the circulator, or whether it can be integrated with the rest of the transceiver components, and the power capability for the transmitting path, as the transmitted signal's power can be very high. It is also certain that broadband circulator designs are always preferred.

1.2 Existing Circulator Types

Although the problems facing to circulators are also issues to other types of duplexers, making a high-quality circulator can be more challenging than a frequency-diplexer, for example. Some of the existing circulator types are discussed here to review their achievements and shortcomings in performance.

1.2.1 Ferrite Circulators

Ferrite is a kind of non-reciprocal material and conventional circulators have been using ferrite till today. One of the classic circulator designs with ferrite dates back to Bosma [1]. A ferrite circulator can have low receiving insertion loss and moderate TX/RX isolation. As it is a passive component, the receiving insertion loss of a ferrite circulator is equivalent to its noise figure. Ferrite circulators are also capable of handling high power. However, they are notorious with their bulky sizes and their narrow operation bandwidths, particularly when

they are operated at the lower end of the microwave frequency spectrum. They are hardly applicable for integrated circuits.

1.2.2 Active Circulators

Active circulators, which utilize the non-reciprocity of transistors, were first proposed by Tanaka, et al. [2] to come to the rescue of low-frequency circulators in integrated circuits (IC), and they have been implemented in MMIC [3]. High-frequency active circulators are also available by using the quasi-circulator modules [4]. An active circulator can have moderate TX/RX isolation over a moderately-wide bandwidth. However, the top concern of active non-reciprocal components is their noise performance, which is generally poor [5–7]. Due to the current IC technology used for active circulators, they are not able to handle high power, but such problem may be resolved soon in the future with the newly-coming, high-bandgap GaN semiconductor.

1.2.3 Photonic Circulators

Recently, Cox and Ackerman have proposed a transmit isolating receive photonic (TIPRx) link [8–10] working as a photonic circulator which has shown a great advantage in TX/RX isolation with a very broad bandwidth over the conventional ferrite and active circulators. As they don't target for IC, photonic circulators are large in size. Their noise performance is also poor [10], though they are claimed to have relatively low-noise performance compared to most of other photonic devices.

1.3 A New Solution: The DMC

It is well known that nonlinear elements like time-varying capacitors can provide frequency mixing for the signals going through them [11] with some relations summarized in [12, 13]. Such feature is utilized to build various frequency converters, including in many recent

works [14–16] where some employ varactors and parametric circuits to improve the noise performance. It turns out that the frequency mixing feature of nonlinear elements may also play a role in a non-reciprocal circuit design, although few works have been done in this area probably due to the lack of a good analytical model for design.

More specifically, it has been recently discovered that nonlinear or time-varying transmission lines (TVTLs), such as a transmission line with time-varying capacitance, can offer a broadband non-reciprocity in the frequency mixing characteristics [17] and they can be used for circulators. Such circulators can provide great TX/RX isolation and low receiving insertion loss comparable to ferrite circulators but with a broader band. Even better, they can be implemented with the modern integrated circuit technology, which may eventually lead to monolithic integration of the complete transceiver front-end.

Based on the TVTL model, we propose a circuit by distributing time-varying shunt capacitors whose capacitances are modulated. We call them as distributedly modulated capacitors and DMC is short for the circuit with those capacitors. The circuit can achieve non-reciprocity and serve for a integrated circulator with good isolation and low insertion loss over a broad band.

1.4 Thesis Outline

In this thesis, a non-reciprocal component made of only transmission lines and time-varying capacitors is envisioned. A circuit with distributedly modulated capacitors (DMC) is introduced. The theory for guiding the DMC design is detailed in Chapter 2. Based on the theory, a specific prototype design is made and described in Chapter 3. After that, results are given and compared in Chapter 4. Finally, Chapter 5 summarizes the findings and suggests some future directions.

CHAPTER 2

Principle of DMC

Transmission lines whose reactance is time-varying have been well studied for many years with some interesting properties. One of the classical applications is the traveling wave parametric amplifier design [18, 19]. The analysis on the time-varying transmission line (TVTL), especially with time-varying capacitance, is reviewed first in Section 2.1.

The theoretical TVTL model can be approached by distributing along a normal transmission line a finite number of variable shunt capacitors, whose capacitances are modulated by a carrier wave that travels in another transmission line at the same phase velocity of the signal waves, as illustrated in Figure 2.1. We call those capacitors as distributedly modulated capacitors and the circuit with them as DMC. It is also shown in Figure 2.1 that non-reciprocity between transmitting and receiving paths can be achieved by comparing the signals at the sidebands of the carrier. More detail is given in Section 2.2.

2.1 Transmission Lines with Time-Varying Capacitance

Figure 2.2 shows a lump-element circuit model for a lossless transmission line with time-varying capacitance. Given the model, the transmission line equations are

$$\frac{\partial v(z,t)}{\partial z} = -L' \frac{\partial i(z,t)}{\partial t}, \tag{2.1a}$$

$$\frac{\partial i(z,t)}{\partial z} = -\frac{\partial [C'(z,t)v(z,t)]}{\partial t}. \tag{2.1b}$$

Rearranging the equations, one can obtain

$$\frac{\partial^2 v(z,t)}{\partial z^2} = L' \frac{\partial^2 [C'(z,t)v(z,t)]}{\partial t^2}. \tag{2.2}$$

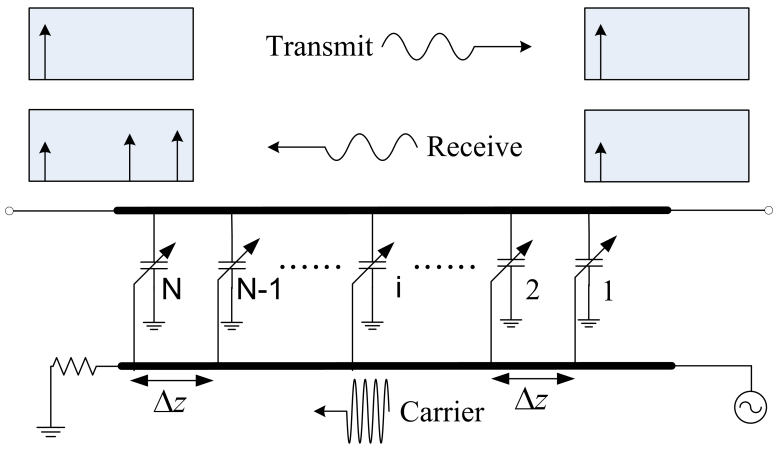

Figure 2.1: Depiction of DMC: the received signal in the same direction of the carrier generates signals at the sidebands of the carrier, while the transmitted signal in the opposite direction does not (See Section 2.2).

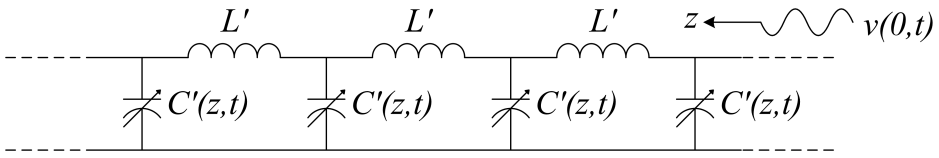

Figure 2.2: A transmission line with time-varying capacitance.

When the capacitance is modulated by a single-tone carrier wave traveling in $+z$ direction at the angular frequency ω_m (the subscript "m" means modulation), it can be written in a general form of

$$C'(z,t) = C'_0 + C'_m \cos(\omega_m t - \beta_m z + \phi_m), \tag{2.3}$$

where C'_0 is the mean capacitance, C'_m is the amplitude of the variation, and β_m is the phase constant of the carrier.

A signal wave launched into this transmission line also in $+z$ direction at the frequency ω_s is mixed up and down with the capacitance modulation frequency ω_m, generating many harmonic and intermodulation terms. As the modulation frequency is normally chosen to be greater than the signal frequency ($\omega_m > \omega_s$), one can limit the discussions to three major tones: the input tone ω_s and the sidebands of the carrier $\omega_{m-s} = \omega_m - \omega_s$ and $\omega_{m+s} = \omega_m + \omega_s$.

Assuming the variation of the capacitance is small and the transmission line is non-dispersive over the bandwidth interested, particularly,

$$\frac{\omega_s}{\beta_s} = \frac{\omega_{m-s}}{\beta_{m-s}} = \frac{\omega_{m+s}}{\beta_{m+s}} = \frac{\omega_m}{\beta_m} = v_p = \frac{1}{\sqrt{L'C'_0}}, \tag{2.4}$$

a solution for (2.2) can be

$$\begin{aligned} v(z,t) = V_s(z)\cos(\omega_s t - \beta_s z + \phi_s) + V_{m-s}(z)\sin(\omega_{m-s}t - \beta_{m-s}z + \phi_m - \phi_s) \\ + V_{m+s}(z)\sin(\omega_{m+s}t - \beta_{m+s}z + \phi_m + \phi_s), \end{aligned} \tag{2.5a}$$

where the amplitudes at the three tones follow

$$V_s(z) = V_0 \cos\left(\frac{1}{2\sqrt{2}}\xi\beta_s z\right), \tag{2.5b}$$

$$V_{m-s}(z) = -\frac{V_0}{\sqrt{2}}\frac{\beta_{m-s}}{\beta_s}\sin\left(\frac{1}{2\sqrt{2}}\xi\beta_s z\right), \tag{2.5c}$$

$$V_{m+s}(z) = -\frac{V_0}{\sqrt{2}}\frac{\beta_{m+s}}{\beta_s}\sin\left(\frac{1}{2\sqrt{2}}\xi\beta_s z\right), \tag{2.5d}$$

and

$$\xi = C'_m/C'_0, \tag{2.5e}$$

given the boundary condition $v(0,t) = V_0\cos(\omega_s t + \phi_s)$ at the source. More detail on the derivation of the solution is provided in Appendix A.

In a word, a signal wave propagating in the same direction and at the same phase velocity of the modulation carrier in the TVTL produces waves at the sidebands of the carrier, whose amplitudes are formulated by (2.5c) and (2.5d). On the other hand, if the signal travels in the opposite direction to the carrier, they interact in a different way and result in no comparable signals at the sidebands. Non-reciprocity can be thus achieved.

2.1.1 Gain of the Receiving Path in the DMC

The DMC bears all the features of a TVTL, including the generation of the signals at the sidebands and the non-reciprocity for the signals traveling in different directions.

If we assign the received signal (RX) to travel in the same direction of the carrier, as shown in Figure 2.1, the RX gain of the DMC can be derived based on (2.5c) or (2.5d). It is worth noting that the output voltage amplitude at the fundamental tone ω_s expressed by (2.5b) is never beyond the input voltage amplitude V_0. For traveling-wave parametric amplifiers [18, 19], exponential amplification at the fundamental tone may be expected with the assumption that the signal at only one of the sidebands, usually ω_{m-s}, are generated. The signal at the upper sideband ω_{m+s} may be cut off by a filter or the transmission line itself. If the lower sideband ω_{m-s} happens to be equal to ω_s, or $\omega_m = 2\omega_s$, the parametric amplifiers belong to a special class called degenerate parametric amplifiers. For broadband application, we assume ω_{m-s} is never equal to ω_s, and in practice, the assumption that the signal at ω_{m+s} is cut off may not be valid. As a result, (2.5) is the notable solution. The signals at the sidebands are utilized and we regard the input signal as being frequency-converted, and then the gain is defined in the same way for a mixer. Given a total length of $z = N\Delta z$ for the DMC, where N is the number of the capacitors and Δz is the distance between adjacent capacitors, the RX gain can be formulated by

$$G_{m\pm s} = 20\log\left|\frac{1}{\sqrt{2}}\frac{\beta_{m\pm s}}{\beta_s}\sin\left(\frac{1}{2\sqrt{2}}\xi\beta_s N\Delta z\right)\right| \quad \text{in dB}, \tag{2.6}$$

where the choice of the sign "$\pm$" depends on which sideband is concerned.

2.2 A Circulator with DMC

Taking the advantage of the non-reciprocity in direction-dependent frequency-conversion, circulators can be developed with DMC to separate the transmitted and received signals even at the same operation frequency. Illustrated in Figure 2.1 reproduced in Figure 2.3, the sideband signal generated from the received signal can be identified by a diplexer at the input of the receiver, and the transmitted signal, which does not have signals at the sidebands, would not be detected by the receiver.

In fact, a small amount of the sideband signal from the transmitted signal inevitably exist. Fortunately, an intuitive analysis described in this section can provide a good prediction on

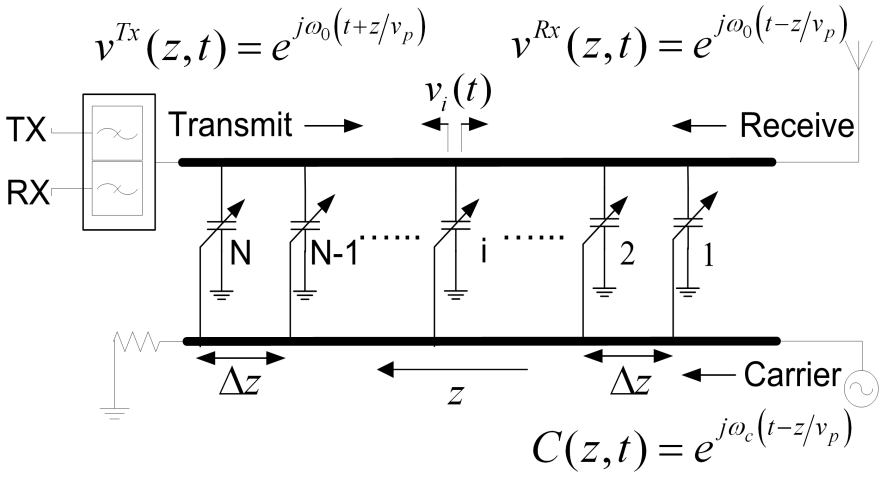

Figure 2.3: DMC for circulator application.

the actual transmitted signal level at the sidebands, and hence the TX/RX isolation can be formulated.

2.2.1 Expressions for the Capacitance and the Signals

As shown in Figure 2.3, N capacitors are distributed along the upper transmission line with equal delay Δz. Their capacitances are modulated by a single-tone carrier wave traveling in $+z$ direction in the lower line. For simplicity, let us consider only the first-order nonlinearity of the capacitors. That is, the relation between their capacitances and the carrier wave can be written as

$$C(v_c) = C_0 + C_1 v_c, \tag{2.7}$$

where the single-tone carrier wave can be represented by

$$v_c(z,t) = V_c \cos(\omega_c t - \beta_c z + \phi_c) = \frac{1}{2} V_c e^{j\phi_c} e^{j\omega_c(t-z/v_p)} + \frac{1}{2} V_c e^{-j\phi_c} e^{-j\omega_c(t-z/v_p)}, \tag{2.8}$$

where ω_c is the carrier's angular frequency and v_p is its phase velocity along the transmission line so that its propagation constant $\beta_c = \omega_c/v_p$. If we emphasis only on the positive-ω_c term that generates the interesting sideband signals and assume the mean capacitance C_0 in (2.7) is zero, or in practice it is considered being embedded into the the transmission line

by using periodic structure analysis (See Section 3.3), then (2.7) becomes

$$C(z,t) = \frac{1}{2}C_1 V_c e^{j\phi_c} \cdot e^{j\omega_c(t-z/v_p)} = A_c e^{j\omega_c(t-z/v_p)}. \tag{2.9}$$

As A_c is constant, (2.9) can be normalized to be simply

$$C(z,t) = e^{j\omega_c(t-z/v_p)}. \tag{2.10}$$

Similar procedures can be followed to write expressions for the received signal (RX) that travels in $+z$ direction and the transmitted signal (TX) in $-z$ direction. It is assumed, unless specified otherwise, that the transmission lines are TEM lines where signals at all frequencies propagate at the same phase velocity. There is even a phase velocity match between the upper and the lower transmission lines shown in Figure 2.3. Given two signals at the same frequency ω_0 with the same amplitude V_0 but in different directions, they can be expressed as

$$v^{RX}(z,t) = V_0 \cos\left(\omega_0 t - \beta_0 z + \phi_0^{RX}\right) = \frac{1}{2}V_0 e^{j\phi_0^{RX}} e^{j\omega_0(t-z/v_p)} + \frac{1}{2}V_0 e^{-j\phi_0^{RX}} e^{-j\omega_0(t-z/v_p)}, \tag{2.11}$$

$$v^{TX}(z,t) = V_0 \cos\left(\omega_0 t + \beta_0 z + \phi_0^{TX}\right) = \frac{1}{2}V_0 e^{j\phi_0^{TX}} e^{j\omega_0(t+z/v_p)} + \frac{1}{2}V_0 e^{-j\phi_0^{TX}} e^{-j\omega_0(t+z/v_p)}. \tag{2.12}$$

Or simply, if we care only about the interesting terms for the following derivation without loss of generality, let us have

$$v^{RX}(z,t) = e^{j\omega_0(t-z/v_p)}, \tag{2.13}$$

$$v^{TX}(z,t) = e^{j\omega_0(t+z/v_p)}. \tag{2.14}$$

Although here we assume the loss of the waves propagating along the transmission line is negligible, an analysis with consideration of such loss, particularly in the carrier, is given in Section 2.2.3.

2.2.2 Derivation of TX/RX Isolation Equation

Without resort to the TVTL theory, another way to think of the DMC is considering the frequency mixing property of discrete nonlinear elements [11–13]. The signal wave in either direction propagating on the upper transmission line in Figure 2.3 mixes with a time-varying capacitor, generating signals at the sidebands that propagate toward both ends of the upper line. The signal at the original frequency continues to propagate with little change caused by the mixing, if multiple-time mixing products are neglected and the energy lost for mixing is small as the capacitor's variation is small. When the received signal is incident from the right side, the signal v_i^{RX} at the sideband $\omega_c + \omega_0$ generated by the ith capacitor is

$$v_i^{RX}(t) = C(i\Delta z, t) \cdot v^{RX}(i\Delta z, t) = e^{j\omega_c(t-i\Delta z/v_p)} e^{j\omega_0(t-i\Delta z/v_p)} = e^{j(\omega_c+\omega_0)(t-i\Delta z/v_p)}. \quad (2.15)$$

The complete expression for v_i^{RX} as a voltage leaving for each end, using the small-signal analysis for nonlinear elements [13], should be

$$\begin{aligned} v_i^{RX}(t) &= Z_0 \cdot \frac{1}{2} i_i^{RX}(t) = Z_0 \cdot \frac{1}{2} j(\omega_c + \omega_0) \frac{1}{2} C_1 V_c e^{j\phi_c} \frac{1}{2} V_0 e^{j\phi_0^{RX}} \cdot e^{j(\omega_c+\omega_0)(t-i\Delta z/v_p)} \\ &= j\frac{1}{8}(\omega_c + \omega_0) Z_0 C_1 V_c V_0 e^{j(\phi_c+\phi_0^{RX})} \cdot e^{j(\omega_c+\omega_0)(t-i\Delta z/v_p)} = A^{RX} e^{j(\omega_c+\omega_0)(t-i\Delta z/v_p)}, \end{aligned} \quad (2.16)$$

where Z_0 is the characteristic impedance of the transmission line. Normalization is made in (2.15) as the constant coefficient A^{RX} will be eventually canceled in (2.22). Using (2.15), the RX signals at $\omega_c + \omega_0$ arriving at both ends accumulate to be

$$v_{left}^{RX}(t) = \sum_{i=1}^{N} v_i^{RX}\left[t - (N-i)\Delta z/v_p\right] = \sum_{i=1}^{N} e^{j(\omega_c+\omega_0)(t-N\Delta z/v_p)} = N e^{j(\omega_c+\omega_0)(t-N\Delta z/v_p)}, \quad (2.17)$$

$$v_{right}^{RX}(t) = \sum_{i=1}^{N} v_i^{RX}(t - i\Delta z/v_p) = \sum_{i=1}^{N} e^{j(\omega_c+\omega_0)(t-2i\Delta z/v_p)} = e^{j(\omega_c+\omega_0)t} \sum_{i=1}^{N} e^{-j2i(\omega_c+\omega_0)\Delta z/v_p}. \quad (2.18)$$

It is expected that the amplitude of the accumulated RX signals at $\omega_c + \omega_0$ arriving at the left end is nonzero. It will be shown in Section 2.2.4 that (2.17) agrees to (2.5d).

Similarly, when the transmitted signal is injected from the left side, the associated signal at the ith capacitor is

$$v_i^{TX}(t) = C(i\Delta z, t) \cdot v^{TX}(i\Delta z, t) = e^{j\omega_c(t-i\Delta z/v_p)} e^{j\omega_0(t+i\Delta z/v_p)} = e^{j[(\omega_c+\omega_0)t-\omega_c i\Delta z/v_p+\omega_0 i\Delta z/v_p]}, \tag{2.19}$$

which is again a normalized expression. If the transmitted signal has the same level as the received signal, the coefficient is canceled in the calculation for TX/RX isolation. The TX signals at $\omega_c + \omega_0$ accumulated at both ends are thus

$$\begin{aligned} v_{left}^{TX}(t) = \sum_{i=1}^{N} v_i^{TX}\left[t-(N-i)\Delta z/v_p\right] &= \sum_{i=1}^{N} e^{j[(\omega_c+\omega_0)t-\omega_c N\Delta z/v_p-\omega_0(N-2i)\Delta z/v_p]} \\ &= e^{j(\omega_c+\omega_0)(t-N\Delta z/v_p)} \sum_{i=1}^{N} e^{j2i\cdot\omega_0\Delta z/v_p}, \end{aligned} \tag{2.20}$$

$$v_{right}^{TX}(t) = \sum_{i=1}^{N} v_i^{TX}(t-i\Delta z/v_p) = \sum_{i=1}^{N} e^{j[(\omega_c+\omega_0)t-\omega_c 2i\Delta z/v_p]} = e^{j(\omega_c+\omega_0)t} \sum_{i=1}^{N} e^{-j2i\cdot\omega_c\Delta z/v_p}. \tag{2.21}$$

The TX signals at the sideband are suppressed at both ends of the transmission line. The TX/RX isolation at the left side, defined with respect to the signals at $\omega_c + \omega_0$, is thus

$$|v_{left}^{TX}/v_{left}^{RX}| = \frac{1}{N}\left|\sum_{i=1}^{N} e^{j2i\cdot\omega_0\Delta z/v_p}\right| = \frac{1}{N}\left|\frac{1-e^{j2N\omega_0\Delta z/v_p}}{1-e^{j2\omega_0\Delta z/v_p}}\right| = \frac{\sin(N\omega_0\Delta z/v_p)}{N\sin(\omega_0\Delta z/v_p)}. \tag{2.22}$$

It can be easily verified that the final isolation expression derived with respect to the other sideband $\omega_c - \omega_0$ (assuming $\omega_c > \omega_0$) should be the same as (2.22). In practice, the assumption that the phase velocity v_p is the same for signals at all frequencies may not be valid, especially for those at the upper sideband $\omega_c + \omega_0$, and the isolation performance associated with $\omega_c - \omega_0$ would be more predictable. It is discussed with more detail in Section 3.4.

The isolation performance of DMC emulates that of the side lobes of an antenna array's radiation pattern. It is interesting that recently it is found that the isolation vs. frequency performance can be shaped and improved by tapering the magnitude of coupling between the signals and the carrier [20].

2.2.3 TX/RX Isolation with Loss in Carrier

The carrier's frequency is usually chosen to be much greater than that of the information signals. In our interested case, the carrier frequency is above 4 GHz, while the information signals can be as low as several hundred megahertz. A practical transmission line usually has more resistive loss at higher frequencies. Therefore, the loss in the carrier might be significant and need be considered. An additional term can be added to (2.10) to take such loss into account:

$$C(z,t) = e^{j\omega_c(t-z/v_p)}e^{-\alpha_c z}, \tag{2.23}$$

where $\alpha_c > 0$ is the attenuation constant. Then (2.17) and (2.20) are modified to be

$$v_{left}^{RX}(t) = \sum_{i=1}^{N} e^{j(\omega_c+\omega_0)(t-N\Delta z/v_p)}e^{-\alpha_c i\Delta z} = e^{j(\omega_c+\omega_0)(t-N\Delta z/v_p)}\sum_{i=1}^{N} e^{-i\cdot\alpha_c\Delta z}, \tag{2.24}$$

$$\begin{aligned} v_{left}^{TX}(t) &= \sum_{i=1}^{N} e^{j[(\omega_c+\omega_0)t-\omega_c N\Delta z/v_p-\omega_0(N-2i)\Delta z/v_p]}e^{-\alpha_c i\Delta z} \\ &= e^{j(\omega_c+\omega_0)(t-N\Delta z/v_p)}\sum_{i=1}^{N} e^{j2i\cdot\omega_0\Delta z/v_p}e^{-i\cdot\alpha_c\Delta z}, \end{aligned} \tag{2.25}$$

Finally, the isolation can be written as

$$\begin{aligned} |v_{left}^{TX}/v_{left}^{RX}| &= \left|\left(\sum_{i=1}^{N} e^{j2i\cdot\omega_0\Delta z/v_p}e^{-i\cdot\alpha_c\Delta z}\right)\Big/\sum_{i=1}^{N} e^{-i\cdot\alpha_c\Delta z}\right| \\ &= \frac{1-e^{-\alpha_c\Delta z}}{1-e^{-N\alpha_c\Delta z}}\left|\frac{1-e^{-N(\alpha_c-j2\omega_0/v_p)\Delta z}}{1-e^{-(\alpha_c-j2\omega_0/v_p)\Delta z}}\right|. \end{aligned} \tag{2.26}$$

2.2.4 Revisiting RX Gain: Conformity with TVTL Theory

With the DMC theory, the RX signal (normalized) at the sideband is expressed by (2.17). Based on the TVTL theory, it is also formulated by (2.5d). Here we want to show that they are equivalent.

The length of each unit Δz is assumed small compared to the wavelength of the signal propagating through the transmission line. Then the varying capacitance C_1 for DMC and

C'_m for TVTL can be related by

$$C'_m \Delta z \approx C_1 V_c, \tag{2.27}$$

where V_c is the voltage amplitude of the carrier defined in (2.8). When ξ defined in (2.5e) is small, (2.5b) becomes $V_s(z) \approx V_0$, validating the low loss at the fundamental tone caused by the mixing. From (2.5) and (2.5d), the signal at the upper sideband becomes

$$\begin{aligned} v_{m+s}(z,t) &\approx -\frac{V_0}{\sqrt{2}} \frac{\beta_{m+s}}{\beta_s} \cdot \frac{1}{2\sqrt{2}} \xi \beta_s z \cdot \sin(\omega_{m+s} t - \beta_{m+s} z + \phi_m + \phi_s) \\ &= j \frac{V_0}{8} \xi \beta_{m+s} z \left[e^{j(\phi_m + \phi_s)} e^{j(\omega_{m+s} t - \beta_{m+s} z)} - e^{-j(\phi_m + \phi_s)} e^{-j(\omega_{m+s} t - \beta_{m+s} z)} \right]. \end{aligned} \tag{2.28}$$

Then combining (2.5e), (2.4), $z = N\Delta z$ and (2.27) into (2.28) leads to

$$v^{RX}_{m+s}(t) = j \frac{N}{8} \omega_{m+s} \sqrt{\frac{L'}{C'_0}} C_1 V_c V_0 \left[e^{j(\phi_m + \phi_s)} e^{j\omega_{m+s}(t - N\Delta z/v_p)} - e^{-j(\phi_m + \phi_s)} e^{-j\omega_{m+s}(t - N\Delta z/v_p)} \right]. \tag{2.29}$$

Finally, replacing $\omega_{m+s} = \omega_m + \omega_s$ with $\omega_c + \omega_0$, ϕ_m with ϕ_c, ϕ_s with ϕ_0^{RX} and noticing that $\sqrt{L'/C'_0} = Z_0$ is the characteristic impedance, the coefficient of the $e^{j\omega_{m+s}(t - N\Delta z/v_p)}$ term in (2.29) is exactly $N \cdot A^{RX}$, where A^{RX} is the normalization constant that appears in (2.16).

CHAPTER 3

Designing a DMC for Experiment

A microstrip prototype made with varactor diodes has been designed to approach the DMC for a circulator application in the frequency range of 500 MHz – 2 GHz. This chapter describes various aspects of the design, including the implementation method, the necessary analysis for assumption validation, the choice of the parameters and the devices, and other issues that may matter. Some simulation results, mainly in matching, are provided to validate the design, but more important results, such as the isolation performance, are delivered without duplication in Chapter 4 for comparisons with measurement results.

Throughout this chapter, we simply call the lower transmission line in Figure 2.1 where the carrier propagates as the carrier line, and the upper transmission line for information signals as the signal line.

3.1 Choice of Time-Varying Capacitors

An intuitive way to implement a time-varying capacitor in DMC is using a cut-off transistor, whose drain capacitance can be varied by the gate voltage. However, the gate and the drain of the transistor are usually not well isolated especially at high frequencies, and great amount of power from the carrier may leak to the signal line, which is not desired. Double-balanced implementation is thus necessary for suppressing the carrier at the signal line (See Section 3.2).

Since double-balanced is used, varactor diodes have then been considered as a better candidate than transistors, as they usually deliver higher variation of capacitance, better

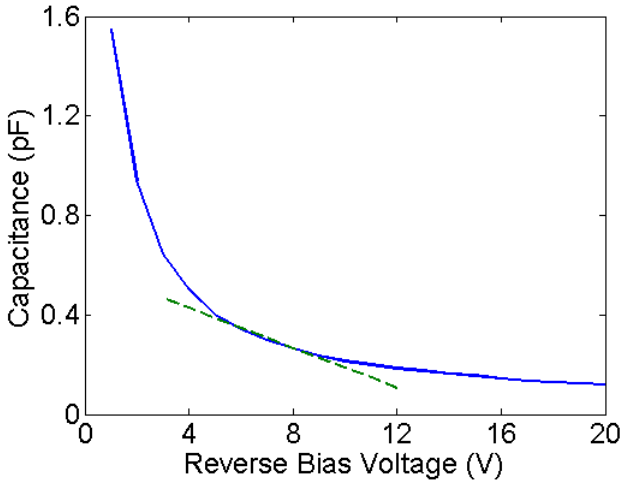

Figure 3.1: C-V curve of the MA46580 varactor [21].

noise performance and easier implementation with double-balanced network. We determine the varactors to be used in our DMC should be with

- Low minimum capacitance,
- High capacitance variation,
- High quality factor or Q value, and
- Few parasitics.

The last two requirements ensure the varactors can work properly at high frequencies. Based on those requirements, we target at the MA46580 varactor from M/A-COM [21].

MA46580 is a beam lead GaAs varactor with a high Q value ($\geq$ 3000 at 4 V, 50 MHz) compared to most of other available varactors. There is little package parasitics and it is reported to be useful at frequencies up to 40 GHz. Figure 3.1 shows the capacitance vs. voltage curve of the MA46580 varactor. The curve is nonlinear as is typical for most varactors. The capacitance of the MA46580 varactor can reach 0.2 pF when it is biased at a high voltage, but the variation there is very limited. The variation at the lower voltage range is greater, but the mean capacitance there is higher. The compromise between high

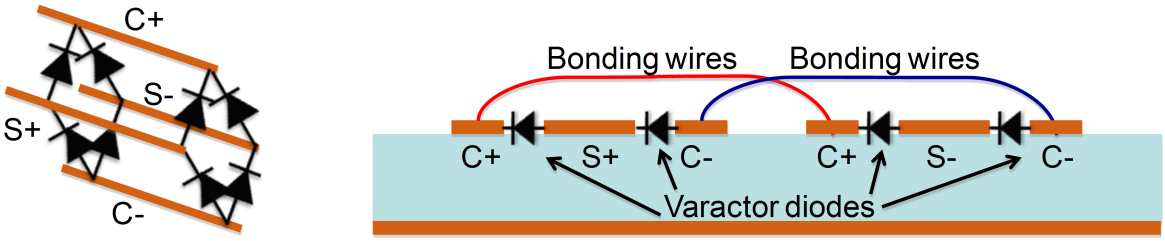

(a) (b)

Figure 3.2: DMC implemented with double balanced network: (a) Ideal 3D illustration; two units are shown. (b) Planar microstrip implementation; the cross section of one unit is shown.

capacitance variation and low mean capacitance leads to the choice of a DC bias around 7 V. The dashed curve in Figure 3.1 shows our desired working range and our approximation on the variation for the varactor, which corresponds to $C_0 = 0.3$ pF and $C_1 = -0.04$ pF/V, where C_0 is the mean capacitance of the varactor at the DC bias and C_1 is the variation of the capacitance per voltage defined in (2.7).

3.2 Double-Balanced Network

To best approach the DMC idea, we propose using the double-balanced network with varactor diodes. Illustrated in Figure 3.2a, pairs of out-of-phase carrier and signal waves propagate on electrically isolated transmission lines. The reversed-biased varactor diodes are in shunt between either of the carrier lines and either of the signal lines. The shunt capacitance is then predominantly controlled by the carrier wave, as it is much stronger than the signal wave. Due to differential symmetry, the carrier wave is not present in the signal lines and thus the isolation of the signal from the carrier is achieved. A planar version of the double-balanced network implemented with microstrip transmission lines is shown in Figure 3.2b.

Independent designs for the carrier lines and for the signal lines are possible with the double-balanced network. Consider the planar implementation in Figure 3.2b, where there are four carrier lines and two signal lines. Each carrier line "sees" only one shunt varactor

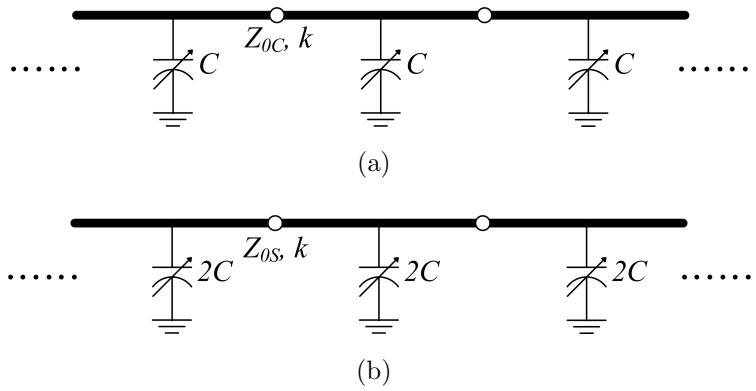

Figure 3.3: Equivalent circuits for (a) each carrier line; (b) each signal line. C represents the capacitance of each varactor.

in each unit, while each signal line "sees" two of them. Equivalent circuits for the carrier line and for the signal line are thus developed as shown in Figure 3.3. In order to match the phase velocity of the waves propagating through them, different characteristics must be assigned for the two lines, as different Z_0's are noted in Figure 3.3. More detail is discussed in the next section.

3.3 Periodic Structure Analysis

As many capacitors are distributed with equal distance, DMC can be treated as a finite periodic structure. In theory, the mean capacitance of each capacitor is assumed zero, but in reality, no varactors have zero mean capacitance. However, we can embed the non-zero mean capacitance into a transmission line using the periodic structure analysis to form an equivalent transmission line without awareness of it.

Illustrated in Figure 3.4, a transmission line with characteristic impedance Z_0 and propagation constant k, if loaded with capacitors of C_0 periodically by a distance of d, is equivalent to a new transmission line with effective impedance Z_B and effective propagation constant β. Equations for Z_B and β in terms of Z_0, kd and C_0 are available in many textbooks [22] and provided here without proof:

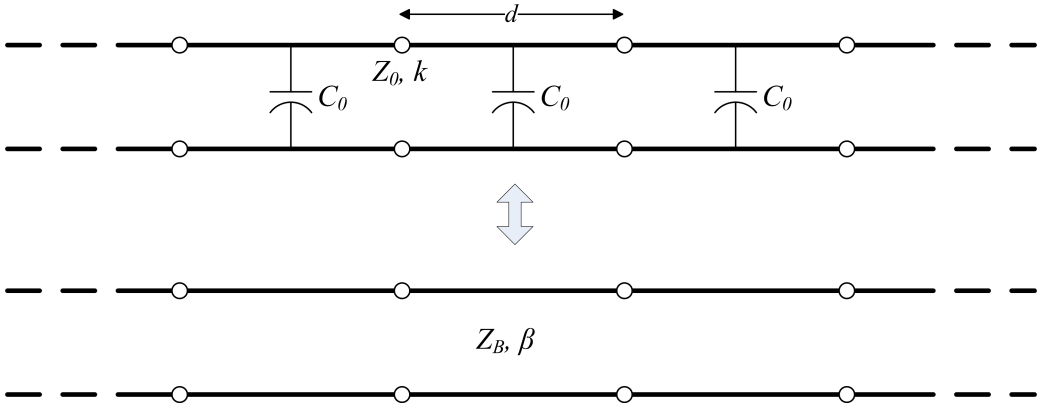

Figure 3.4: Transforming a periodic structure into an equivalent transmission line.

$$\cos(\beta d) = A = \cos(kd) - \frac{\omega C_0 Z_0}{2}\sin(kd), \tag{3.1a}$$

$$Z_B = \frac{BZ_0}{\sqrt{1-A^2}}, \tag{3.1b}$$

where

$$B = \sin(kd) + \frac{\omega C_0 Z_0}{2}[\cos(kd) - 1]. \tag{3.1c}$$

It is expected that both Z_B and β are dependent on the frequency ω, which suggests that the equivalent transmission line is dispersive in general. This limits the useful frequency range where our assumption is valid that the line is nearly non-dispersive.

Given $kd = \pi/2$ or 90° with respect to the phase delay of a 6 GHz signal through the unloaded line in each unit and $C_0 = 0.3$ pF as given in Section 3.1, one can plot the effective impedance or Bloch impedance Z_B and the effective phase delay through each unit βd of the carrier line and the signal line by referring to the models in Figure 3.3. Additional information, namely $C = C_0$, $Z_{0C} = 125\ \Omega$ and $Z_{0S} = 62.5\ \Omega$, is used for the plots in Figure 3.5. Notice that beyond a certain frequency, both Z_B and βd become purely imaginary, which physically means the wave stops propagating through such periodic structure, if its frequency is higher than this so-called cutoff frequency associated with the periodic structure. In our design, the cutoff frequency is around 6.8 GHz. For waves below 5 GHz, βd is approximately proportional to the frequency, where the periodic structure can be considered as non-dispersive, i.e. the waves propagate through it at the same phase velocity.

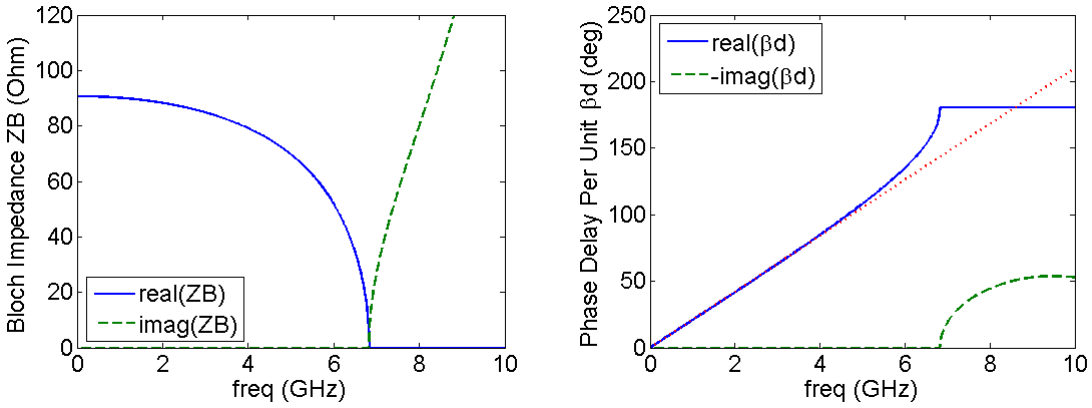

(a) For each carrier line.

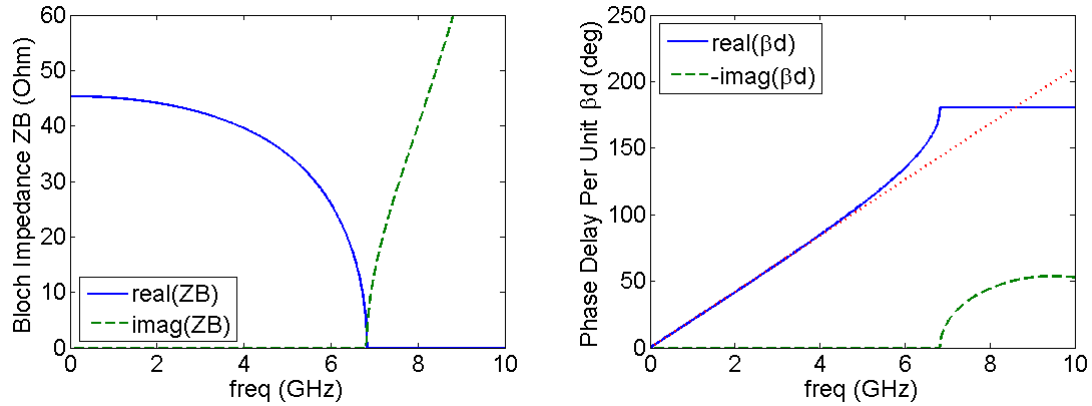

(b) For each signal line.

Figure 3.5: Effective characteristics of the periodic structures.

Additional comments need be made on the selection of the values for the design. One of our original ideas is using a 6 GHz carrier and that is why kd is specified with respect to 6 GHz. Another original idea is to match the signal line to 50 Ω at frequencies below 2 GHz, which require a higher Z_{0S} than 62.5 Ω. However, a high Z_{0S} conflicts with a high cutoff frequency. Moreover, as there are two capacitors in shunt of the signal line in each unit while there is only one for the carrier line, it is required that $Z_{0C} = 2Z_{0S}$ in order to match the phase velocities of the waves propagating through the carrier line and the signal line. A higher Z_{0S} makes Z_{0C} even higher and eventually the microstrip line for the carrier can

be too thin to be fabricated or useful based on most of the substrates available. Therefore, compromise has been made and $Z_{0C} = 125\ \Omega$ is chosen and then $Z_{0S} = 62.5\ \Omega$ is determined. The choice of the carrier frequency is further discussed in the next section.

3.4 Choice of Carrier Frequency

It is assumed in our theory that signals at both sidebands of the carrier should not be cutoff. In fact, the signals at the fundamental tone and at both sidebands should propagate at the same phase velocity, which requires the carrier frequency should be much lower than the cutoff frequency. In addition, it is implied that the fundamental tone and the sidebands should not overlap.

Based on the current design, the cutoff frequency of the periodic structures is around 6.8 GHz. The operation frequency range that we target at is 0.5 – 2 GHz. Therefore, in order to have the signal at the upper sideband survive, the carrier frequency must be below 4.8 GHz. To avoid the overlap between the fundamental tone and the lower sideband, the carrier frequency must be above 4 GHz. There is not much room left for choosing the carrier frequency. The final value is settled around 4.2 GHz. Notice that, however, the phase velocity of the signal at the upper sideband is faster than those at the fundamental tone and at the lower sideband, as indicated by Figure 3.5 that βd bends up starting from around 4.2 GHz. As a result, the theory fails to predict the performance with respect to the upper sideband in the current design.

3.5 Choice of Substrate

The substrate chosen for prototype is Rogers RO4003C [23]. The material is suitable for high frequency application. Some important data about the substrate we use are listed in Table 3.1. The circuit layout made on this substrate is easy for etching, but the carrier lines are so thin that they may be lossy as the tangent loss of the material is not extremely low.

Substrate thickness h:	32 mil
Relative dielectric constant ϵ_r:	3.55
Relative permeability μ_r:	1
Conductor conductivity:	5.8×10^7 S/m
Conductor thickness:	35 µm
Dielectric loss tangent $\tan\delta$:	0.0027

Table 3.1: Data of the Rogers RO4003C substrate [23].

3.6 Design of Unit Cell

The unit cell composes of two carrier lines and one signal line with two varactors in shunt between them. With the substrate determined, the dimensions of the microstrip transmission lines in each unit are calculated and displayed in Figure 3.6, where the dimensions of the varactors are also included. A Momentum simulation is performed in ADS on the layout. Figure 3.7 checks the phase delays of the carrier line and the signal line through the unit cell. It shows that the delays are about the same, indicating the same velocity that signals propagating through the lines.

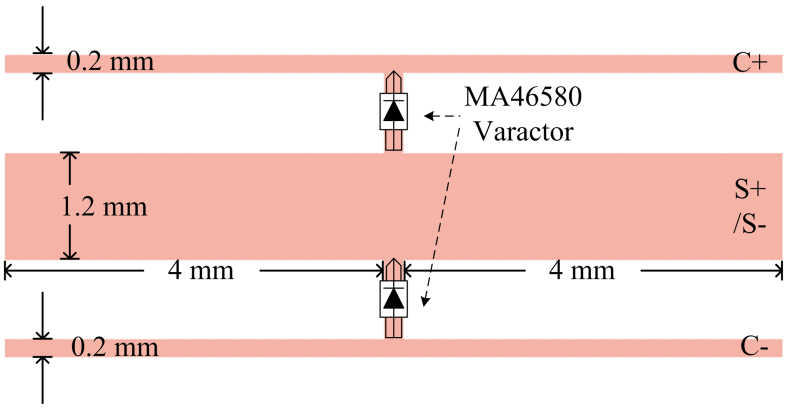

Figure 3.6: Layout of each unit cell.

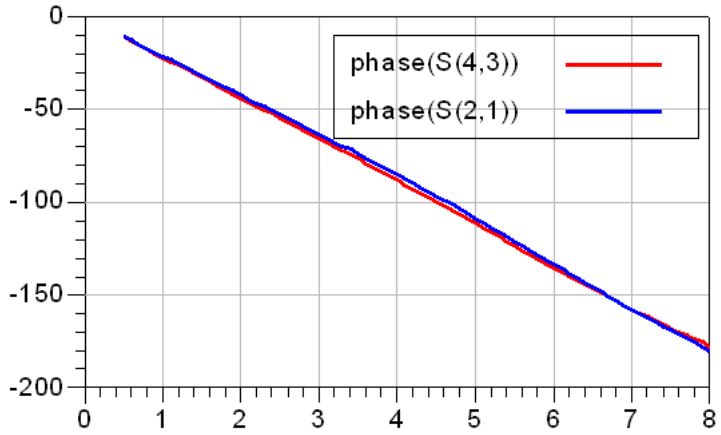

Figure 3.7: Phase matching between the carrier line (S(2,1)) and the signal line (S(4,3)).

3.7 Design of the Ends of the Lines

Figure 3.9 shows the photo of the final prototype consisting of two rows of $N = 16$ unit cells cascading side by side. At either end of the lines, a network is built to combine the common carrier lines and lead all the lines to some 50 Ω ports, as illustrated in Figure 3.8.

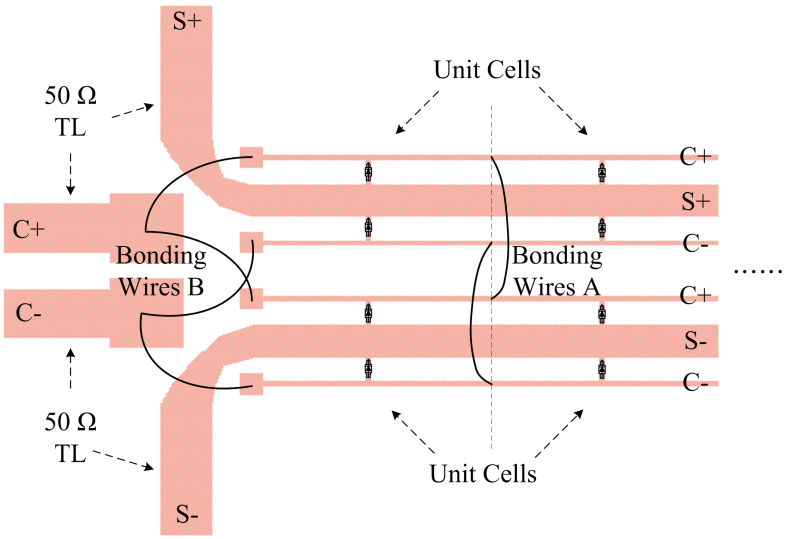

Figure 3.8: Layout of the network at the left end of the lines.

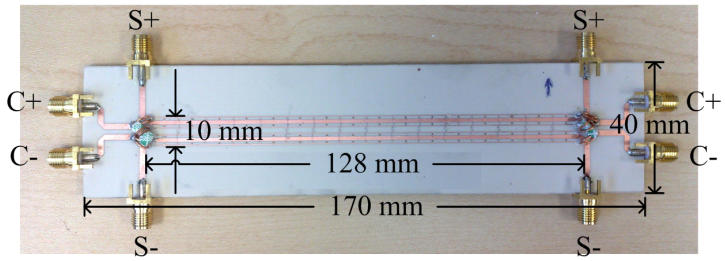

Figure 3.9: Picture of the final prototype.

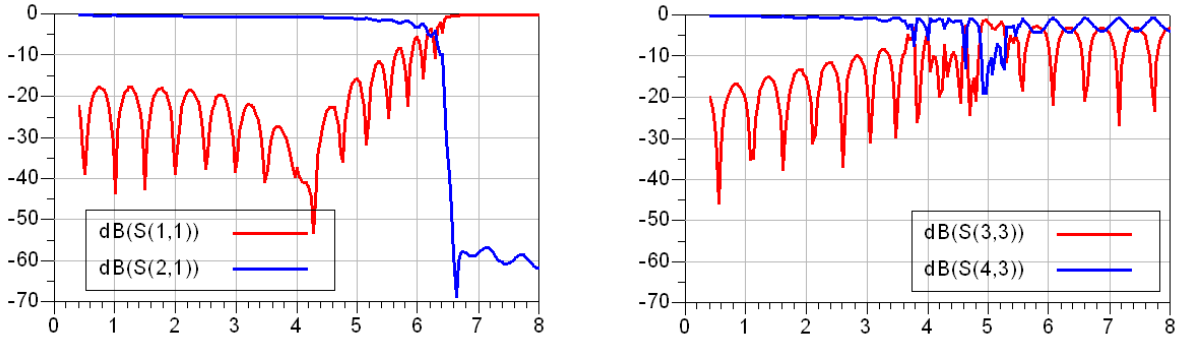

(a) For the carrier path.

(b) For the signal path.

Figure 3.10: Simulated results of the return loss (S(1,1), S(3,3)) and the insertion loss (S(2,1), S(4,3)) of the prototype. Ideal baluns are used to provide differential input pairs.

3.8 Effects of Bonding Wires

Shown in Figure 3.8, the common carrier lines are connected by bonding wires, which in practice have some parasitics, mainly inductance, that may cause problems especially for the high-frequency carrier. The bonding wires A have little effects as they are effectively invisible to the carrier line, but the bonding wires B are in series of the whole carrier paths and their parasitics must be taken into account. Thick wires are employed as they introduce less parasitics than the thin ones, and patches are added at the ends of the bonding wires to help reduce their effects. With an estimation of 2 nH for each bonding wire B (in practice, two parallel copper wires of 1 mm diameter are used to form each 2-nH bonding wire), the simulated return loss and insertion loss of the whole carrier path are plotted in Figure 3.10a.

A notch in the return loss around 4.2 GHz and a cutoff in the insertion around 6.4 GHz are expected and confirmed by the plots. The simulated results for the signal path are also provided in Figure 3.10b. Since the Bloch impedance of the signal line is slightly smaller than 50 Ω at 0.5 – 2 GHz, the matching is not perfect. The cutoff seems disappear, because for high frequency, the bonding wires A comes into effect for the signal lines, though they do not influence the high-frequency carrier and the low-frequency signals in real application.

CHAPTER 4

Performance of the Experimental DMC

The design described in the previous chapter has been fabricated and shown in Figure 3.9 on page 25. Its performance, especially the TX/RX isolation and the RX gain, has been evaluated and compared to the theoretical results. In this chapter, the measurement setup is described and the comparison results are shown.

4.1 Choice of Baluns

As differential inputs are required for the double-balanced network, baluns are necessary and turn out to be crucial for the evaluation of our DMC design. The balun is a balanced-unbalanced transformer that can transform between a single-ended (unbalanced) signal and a differential (balanced) pair. A broadband balun design is also challenging. With our current research focus, we assume baluns with lossless insertion and perfect matching at all ports for our theory and even for simulation. In reality, however, problems with practical baluns need be addressed.

For the carrier inputs, we use a 180° hybrid with the Σ port terminated to serve as the balun. The carrier input is connected to the hybrid's Δ port and its rest ports are for the DMC. Though the balun for the carrier does not need to be broadband, the hybrid has well-matched ports and flat 3 dB Δ-Output insertion loss over its nominal frequency range of 2 – 18 GHz, which covers the 4.2 GHz carrier frequency.

Two baluns are required for the signal paths and they have to be broadband, which should cover not only the signal's input frequency range, but also the range of its sidebands

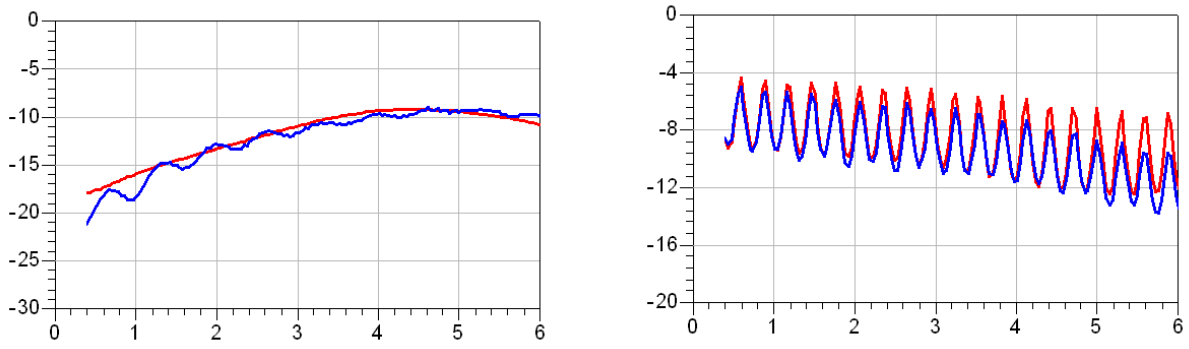

(a) (b)

Figure 4.1: Characteristics of the balun, simulation (red) and measurement (blue): (a) Return loss of the differential port; (b) Insertion loss of the back-to-back connected balun pair.

of the carrier. The input frequency range is 0.5 – 2 GHz, below the operation band of the hybrid for the carrier. In fact, there are few hybrids available that can cover such a wide band. Therefore, different baluns from the hybrid are used for the signal paths.

Marki Microwave's BAL-0006 is a broadband 3-port balun with a nominal frequency range of 200 kHz – 6 GHz [24], which covers the frequency range that we need for the signal paths. However, Figure 4.1a shows there is still some mismatch in the differential ports of this balun confirmed by measurement, and it causes fluctuation shown in Figure 4.1b when we investigate the insertion loss of two baluns connected back-to-back. For measurement of the balun pair, additional cables are employed for connection, and their phase-delay effect is included in the plots in Figure 4.1b. The fluctuation suggests the reflected waves caused by the mismatch greatly interactive with the incident waves and they must be suppressed. Therefore, some 19.5 dB attenuators are loaded at the differential ports to reduce the effects of the mismatch in the later experiment.

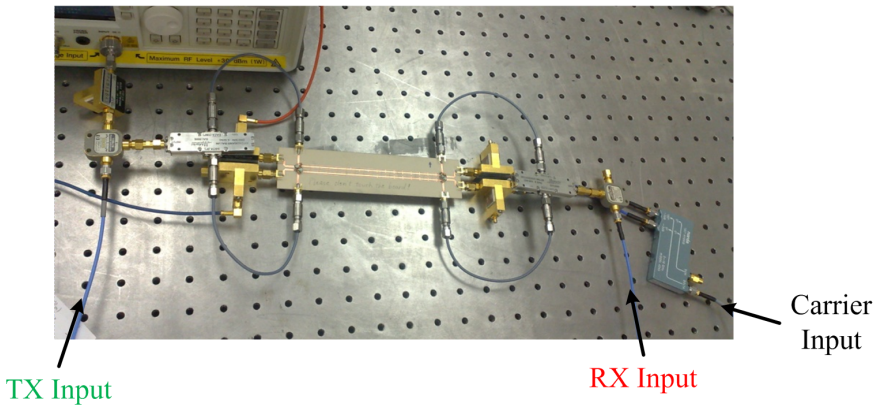

Figure 4.2: Picture of the measurement setup.

4.2 Measurement Setup

Figure 4.2 shows a picture of our measurement setup and Figure 4.3 explains the detail of the connection. The instruments and the components involved in measurement are listed in Table 4.1. During the experiment, the varactor diodes are biased at 7.15 V. A 4.23 GHz, 26 dBm carrier is sent into the DMC. A splitter is used at the TX-input side to provide a path connecting to the spectrum analyzer monitoring the signals at that side. For symmetry, the other splitter is added at the RX-input side with the port terminated by simply a 50 Ω load. The broadband baluns for the signal path include the attenuators at the differential ports to suppress the mismatch problem as mentioned in the previous section.

4.3 RX Gain Measurement

Referring to Section 2.1.1, the receiving (RX) gain is defined as the ratio of the RX output level at the sidebands reaching to the TX-input side over the RX input level at the fundamental tone. Equations (2.5d) and (2.17) provide two ways to express the RX signals at the upper sideband which have been shown equivalent in Section 2.2.4. One may conclude from comparing (2.5c) and (2.5d) that the signal has a greater gain at the upper sideband than at the lower one, while in our prototype, it is not the case for the reason given in Sec-

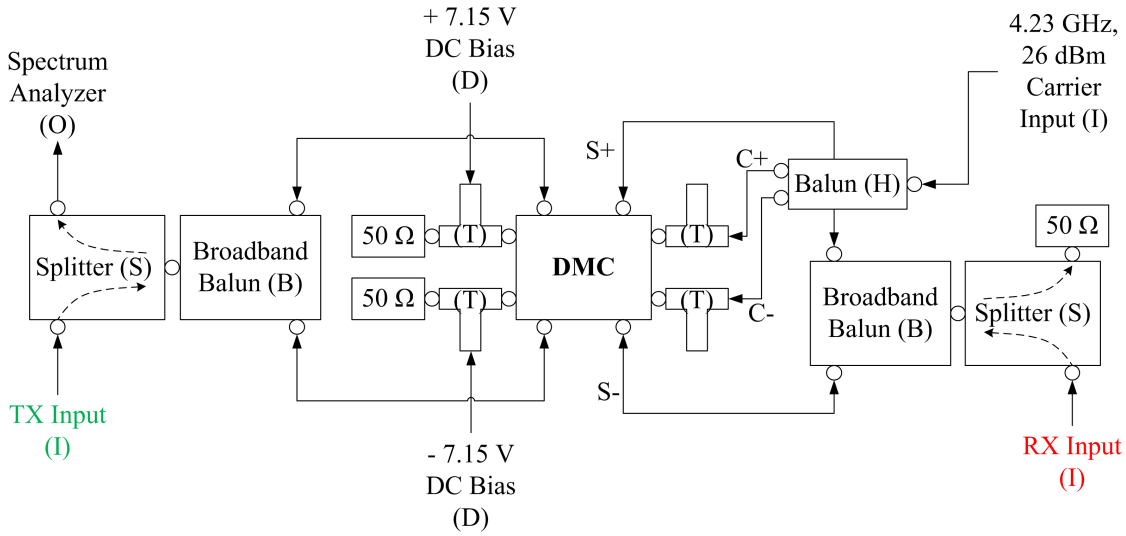

Figure 4.3: Diagram of the measurement setup.

Label	Name	Model Number	Nominal Frequency Range
I	Synthesized Sweeper	HP 8340A	10 MHz – 26.5 GHz
O	Spectrum Analyzer	Agilent 8565EC	9 kHz – 26.5 GHz
D	DC Power Supply	Agilent E3620A	N/A
T	Bias Network	HP 11612A	45 MHz – 26.5 GHz
S	Power Splitter	HP 11667B	DC – 26.5 GHz
H	180° Hybrid	Narda 4346	2 GHz – 18 GHz
B	Broadband Balun	Marki BAL-0006	200 kHz – 6 GHz

Table 4.1: List of the instruments and the components involved in measurement. Refer the labels to Figure 4.3.

tion 3.4. The RX gain associated with the lower sideband is evaluated here to provide the verification of the theory. Reproducing (2.6) with mere consideration of the lower sideband, the theoretical RX gain should be

$$Gain = 20 \log \left| \frac{1}{\sqrt{2}} \frac{\omega_c - \omega_0}{\omega_0} \sin \left(\frac{N}{2\sqrt{2}} \xi \beta_0 \Delta z \right) \right| \quad \text{in dB.} \tag{4.1}$$

Here I use the same notation ω_c and ω_0 as that for the DMC theory instead of ω_m and ω_s for the TVTL theory. Given the assumption and the fact that the signals in question propagate at the same phase velocity, we have $(\beta_c - \beta_0)/\beta_0 = (\omega_c - \omega_0)/\omega_0 = (f_c - f_0)/f_0$. The current DMC is composed of $N = 16$ units (though each unit has two unit cells). $\beta_0 \Delta z$ is the effective phase delay of each unit, which can be determined by the periodic structure analysis. The last thing is thus to estimate the capacitance variation ratio ξ.

4.3.1 Estimation of ξ

The variation ratio of the capacitance ξ is defined by (2.5e) in TVTL theory and for the current design, it is estimated by

$$\xi = \frac{C'_m}{C'_0} = \frac{C'_m \Delta z}{C'_0 \Delta z} \approx \frac{2C_1 V_c}{2C_0 + C'_{0S} \Delta z}, \tag{4.2}$$

where C_0 and C_1 are from the varactors, C'_{0S} is the unit-length capacitance of the signal line, and V_c is the voltage amplitude of the carrier. Recall that two varactors are in shunt of the signal line (See Figure 3.3b) and thus C_0 and C_1 are multiplied by 2. $C'_{0S} \Delta z$ as a whole can be estimated by

$$C'_{0S} \Delta z = \frac{k \Delta z}{\omega Z_{0S}}. \tag{4.3}$$

Recall in Section 3.3 that $k\Delta z = \pi/2$ with respect to $f = 6$ GHz and $Z_{0S} = 62.5\ \Omega$, we have $C'_{0S} \Delta z = 0.667$ pF. Another way is to estimate $C'_0 \Delta z \approx 2C_0 + C'_{0S} \Delta z$ as a whole by

$$C'_0 \Delta z = \frac{\beta \Delta z}{\omega Z_{BS}}, \tag{4.4}$$

where $\beta \Delta z$ is the effective phase delay through each unit with respect to the frequency ω and Z_{BS} is the Bloch impedance of the signal line as a periodic structure. The result is the

same as $2C_0 + C'_{0S}\Delta z$ except the value goes up when the frequency increases. Given the carrier input power of 26 dBm during the experiment, considering the splitting and the loss, the power reaching to each of the four carrier lines is about $P_c = 19.5$ dBm. Then V_c can be estimated by $V_c = \sqrt{2P_cZ_{BC}}$, where Z_{BC} is the Bloch impedance of each carrier line at the carrier frequency. Finally, we have $|\xi| \approx 0.18$ over the signal's input frequency range. The calculated RX gain is thus plotted in Figure 4.4 as the theoretical result.

4.3.2 Calibration in the Measurement

Based on the setup in Figure 4.3, we can measure the RX gain by turning on the RX input and reading the tone at the lower sideband in the spectrum analyzer. The TX input is off, or for symmetry and precision, it can be replaced by a 50 Ω terminator. Since we are interested in the RX gain only through the DMC, the external loss which would be measured needs to be excluded. Namely, the loss through the splitters and the broadband baluns in the signal path should be taken out in the measured result. It is worth mentioning that loss at two frequencies in minimum needs to be determined for each input frequency. For the splitter and the balun connecting to the RX input, the loss is defined at the input frequency, while for those to the spectrum analyzer, it should be determined at the lower sideband.

4.3.3 Comparison of Results

The measured RX gain is summarized and compared with the theoretical result in Figure 4.4. Also included is the simulation result based on the layout described in Chapter 3 and the setup. The loss through the splitters and the baluns in the signal path is excluded in the measured result. In simulation, ideal baluns are used to create the differential inputs. There is a great agreement between the results, especially the decreasing trend in overall of the RX gain curve with respect to the increasing frequency, except that there is still some fluctuation in the measured result due to the mismatch of the baluns. Based on the current design and the setup, small gain is achievable at frequencies below 700 MHz. The loss of the DMC can

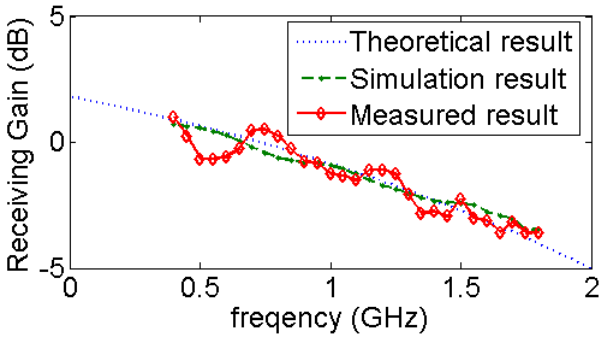

Figure 4.4: The RX gain results.

be controlled within 5 dB throughout the frequency range of 0.7 – 1.8 GHz.

4.4 TX/RX Isolation Measurement

The TX/RX isolation of the DMC is defined as the ratio of the frequency-converted TX level reflected to the TX-input side over the converted RX level reaching there, where the TX and RX inputs are the same (at the same frequency and with the same level). The isolation defined in this way should be negative in dB. Saying a high isolation is equivalent to saying the isolation is greatly negative in dB. By meaning "converted", we are supposed to measure the signals at one of the sidebands, and for the same reason for RX gain measurement, we choose the lower sideband for experiment. In the introduction, the isolation of a circulator seems defined as the TX level leaked to the receiver over the TX input level from the transmitter, and what we define is more properly called directivity of the circulator in some literature. Despite the difference in that the directivity takes the RX gain or loss into account, especially for active circulators, while the conventional isolation does not, they are equally appropriate to describe the non-reciprocal performance of a circulator in the transceiver application.

The calculation of the theoretical TX/RX isolation is quite straightforward from (2.22) and reproduced here:

$$Isolation = 20\log\left|\frac{\sin(N\beta_0\Delta z)}{N\sin(\beta_0\Delta z)}\right| \quad \text{in dB.} \tag{4.5}$$

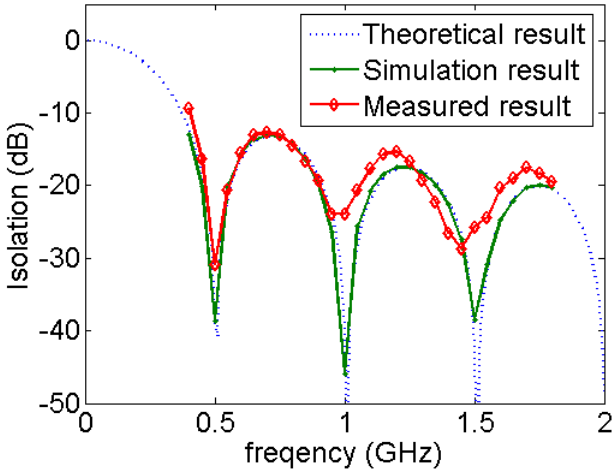

Figure 4.5: The TX/RX isolation results.

Again, $N = 16$ and $\beta_0 \Delta z$ can be calculated by the periodic structure analysis.

To measure the isolation, we can first turn on the RX input and read the sideband signal; then turn off the RX and turn on the TX input, which has the same frequency and the same power level as the RX, to measure the sideband signal again. The two results can be measured in dB and their difference tells the isolation. No calibration is necessary because of the symmetry, assuming the splitters and the broadband baluns are identical, which in practice nearly are.

4.4.1 Comparison of Results

The measured TX/RX isolation is compared with the theoretical and simulation result in Figure 4.5. The side-lobe pattern is observed and the measured result matches well with the others at 0.4 – 1 GHz. In overall, larger than 13 dB isolation over 0.45 – 1.8 GHz is expected and confirmed.

CHAPTER 5

Conclusion

5.1 Summary

This work presents an interesting idea of utilizing non-reciprocity of the time-varying transmission line (TVTL) model. A circuit with distributedly modulated capacitors (DMC) has been proposed to approach the model and serve for a non-reciprocal microwave component such as a circulator. The DMC does not require ferrite and it would be readily integrated into a complete transceiver front-end even at the lower end of the microwave frequency spectrum. The theoretical analysis provides guidelines of RX gain and TX/RX isolation derivations. A microstrip prototype on Rogers substrate using the double-balanced network of GaAs varactor diodes has been designed and tested to verify the theory. Larger than 13 dB isolation with less than 5 dB receiving loss is expected and observed over 500 MHz – 1.8 GHz during the experiment.

5.2 Future Work

There are several aspects of work that can be done to further explore the potential of DMC. The first is to improve the TX/RX isolation performance by using the non-uniform implementation of DMC. The theoretical study has shown even 40 dB isolation is achievable by taping the capacitors' variations [20]. Second, the noise performance of DMC needs to be evaluated. Compared to conventional active non-reciprocal components, we use reverse-biased varactor diodes instead of amplified-transistors, and the varactor's ohmic loss can be

very low given its high-Q value, implying little additional noise introduced. Varactor-based circuits have shown great noise performance, including in the recent parametric amplifier design [25, 26]. Last but not least, the power handling of DMC needs to be investigated. A more robust design using alumina substrate and without using long bonding wires is also considered in the next step.

APPENDIX A

Derivation of the TVTL Solution

Selected details on solving the TVTL equation (2.2) with (2.3) are demonstrated here. Similar steps to those in [18] are taken to derive the solution, but time-varying capacitance, instead of time-varying inductance in [18], is assumed in our case. Signals at three frequencies, the original frequency and both sidebands, are involved in derivation. Rewrite (2.3) into the form of

$$C'(z,t) = C'_0 + C'_m(z,t), \tag{A.1}$$

where

$$\begin{aligned} C'_m(z,t) = C'_m \cos(\omega_m t - \beta_m z + \phi_m) &= \frac{1}{2}C'_m e^{j\phi_m} e^{-j\beta_m z} e^{j\omega_m t} + \frac{1}{2}C'_m e^{-j\phi_m} e^{j\beta_m z} e^{-j\omega_m t} \\ &= \frac{1}{2}C'_m(z)e^{j\omega_m t} + \frac{1}{2}C'^{*}_m(z)e^{-j\omega_m t}, \end{aligned} \tag{A.2}$$

where

$$C'_m(z) = C'_m e^{j\phi_m} e^{-j\beta_m z}, \tag{A.3}$$

is the phasor form of $C'_m(z,t)$ and the superscript "$*$" denotes the complex conjugate. Further, denote

$$\xi = C'_m / C'_0, \tag{A.4}$$

as the ratio of the capacitance variation to the mean capacitance of the transmission line. Inserting (A.1) into (2.2) yields

$$\frac{\partial^2 v(z,t)}{\partial z^2} = L'C'_0 \frac{\partial^2 v(z,t)}{\partial t^2} + L' \frac{\partial^2 [C'_m(z,t)v(z,t)]}{\partial t^2}. \tag{A.5}$$

Given a signal at the frequency ω_s, the signals generated at the sidebands of the modulation carrier, $\omega_{m-s} = \omega_m - \omega_s$ and $\omega_{m+s} = \omega_m + \omega_s$, are of the most significance. Let

$$v_s(z,t) = V_s(z)e^{j\omega_s t} + V_s^*(z)e^{-j\omega_s t}, \tag{A.6a}$$

$$v_{m-s}(z,t) = V_{m-s}(z)e^{j\omega_{m-s} t} + V_{m-s}^*(z)e^{-j\omega_{m-s} t}, \tag{A.6b}$$

$$v_{m+s}(z,t) = V_{m+s}(z)e^{j\omega_{m+s} t} + V_{m+s}^*(z)e^{-j\omega_{m+s} t} \tag{A.6c}$$

represent the signals at the three tones. Inserting (A.2) and (A.6) into (A.5) leads to

$$\frac{d^2V_s(z)}{dz^2} = -\omega_s^2 L'C_0'V_s(z) - \frac{1}{2}\omega_s^2 L'C_m'(z)V_{m-s}^*(z) - \frac{1}{2}\omega_s^2 L'C_m'^*(z)V_{m+s}(z), \tag{A.7a}$$

$$\frac{d^2V_{m-s}^*(z)}{dz^2} = -\omega_{m-s}^2 L'C_0'V_{m-s}^*(z) - \frac{1}{2}\omega_{m-s}^2 L'C_m'^*(z)V_s(z), \tag{A.7b}$$

$$\frac{d^2V_{m+s}(z)}{dz^2} = -\omega_{m+s}^2 L'C_0'V_{m+s}(z) - \frac{1}{2}\omega_{m+s}^2 L'C_m'(z)V_s(z). \tag{A.7c}$$

There are three more equations which are paired in complex conjugate with (A.7).

Now suppose all the signals are traveling in the same direction of the carrier. Then we can assume

$$V_s(z) = A_s(z)e^{-j\beta_s z}, \tag{A.8a}$$

$$V_{m-s}^*(z) = A_{m-s}^*(z)e^{j\beta_{m-s} z}, \tag{A.8b}$$

$$V_{m+s}(z) = A_{m+s}(z)e^{-j\beta_{m+s} z}. \tag{A.8c}$$

Suppose the transmission line is non-dispersive over a broad band, that is,

$$\frac{\omega_s}{\beta_s} = \frac{\omega_{m-s}}{\beta_{m-s}} = \frac{\omega_{m+s}}{\beta_{m+s}} = \frac{\omega_m}{\beta_m} = v_p = \frac{1}{\sqrt{L'C_0'}}, \tag{A.9}$$

which indicates that

$$\beta_{m\pm s} = \beta_m \pm \beta_s. \tag{A.10}$$

When the ratio ξ defined in (A.4) is small, as is generally true in actual applications, $A(z)$'s in (A.8) are slowly varying functions and the terms involving $d^2A(z)/dz^2$ may be neglected. Then substituting (A.3), (A.4) and (A.8) into (A.7), we have

$$-2j\beta_s\frac{dA_s(z)}{dz} - \beta_s^2 A_s(z) = -\omega_s^2 L'C_0'A_s(z) - \frac{1}{2}\omega_s^2 L'C_0'\xi e^{j\phi_m}A_{m-s}^*(z) - \frac{1}{2}\omega_s^2 L'C_0'\xi e^{-j\phi_m}A_{m+s}(z), \tag{A.11a}$$

$$2j\beta_{m-s}\frac{dA^*_{m-s}(z)}{dz} - \beta^2_{m-s}A^*_{m-s}(z) = -\omega^2_{m-s}L'C'_0A^*_{m-s}(z) - \frac{1}{2}\omega^2_{m-s}L'C'_0\xi e^{-j\phi_m}A_s(z), \tag{A.11b}$$

$$-2j\beta_{m+s}\frac{dA_{m+s}(z)}{dz} - \beta^2_{m+s}A_{m+s}(z) = -\omega^2_{m+s}L'C'_0A_{m+s}(z) - \frac{1}{2}\omega^2_{m+s}L'C'_0\xi e^{j\phi_m}A_s(z). \tag{A.11c}$$

Using (A.9) that $\beta^2 = \omega^2 L'C'_0$, the equations are reduced to

$$\frac{dA_s(z)}{dz} = -\frac{1}{4}j\beta_s\xi e^{j\phi_m}A^*_{m-s}(z) - \frac{1}{4}j\beta_s\xi e^{-j\phi_m}A_{m+s}(z), \tag{A.12a}$$

$$\frac{dA^*_{m-s}(z)}{dz} = \frac{1}{4}j\beta_{m-s}\xi e^{-j\phi_m}A_s(z), \tag{A.12b}$$

$$\frac{dA_{m+s}(z)}{dz} = -\frac{1}{4}j\beta_{m+s}\xi e^{j\phi_m}A_s(z). \tag{A.12c}$$

Combining the equations (A.12) with (A.10), we have

$$\frac{d^2A_s(z)}{dz^2} + \frac{1}{8}\xi^2\beta^2_sA_s(z) = 0, \tag{A.13}$$

whose solution in general can be

$$A_s(z) = c_1e^{\gamma z} + c_2e^{-\gamma z}, \tag{A.14a}$$

where

$$\gamma = j\frac{1}{2\sqrt{2}}\xi\beta_s, \tag{A.14b}$$

and c_1, c_2 are complex constants to be determined by the boundary conditions. From (A.12), we also have

$$A^*_{m-s}(z) = \frac{1}{\sqrt{2}}\frac{\beta_{m-s}}{\beta_s}e^{-j\phi_m}\left(c_1e^{\gamma z} - c_2e^{-\gamma z}\right) + c_3e^{-j\phi_m}, \tag{A.14c}$$

$$A_{m+s}(z) = -\frac{1}{\sqrt{2}}\frac{\beta_{m+s}}{\beta_s}e^{j\phi_m}\left(c_1e^{\gamma z} - c_2e^{-\gamma z}\right) - c_3e^{j\phi_m}, \tag{A.14d}$$

where c_3 is another constant to be determined. Put (A.14) into (A.8) and then into (A.6). The boundary conditions are

$$v_s(0,t) = V_0\cos(\omega_st + \phi_s) = \frac{1}{2}V_0e^{j\phi_s}e^{j\omega_st} + \frac{1}{2}V_0e^{-j\phi_s}e^{-j\omega_st}, \tag{A.15a}$$

$$v_{m-s}(0,t) = 0, \tag{A.15b}$$

$$v_{m+s}(0,t) = 0. \tag{A.15c}$$

The constants are thus

$$c_1 = c_2 = \frac{1}{4} V_0 e^{j\phi_s}, \quad c_3 = 0. \tag{A.16}$$

Finally, the solution is

$$v_s(z,t) = V_0 \cos\left(\frac{1}{2\sqrt{2}}\xi\beta_s z\right)\cos(\omega_s t - \beta_s z + \phi_s), \tag{A.17a}$$

$$v_{m-s}(z) = -\frac{V_0}{\sqrt{2}}\frac{\beta_{m-s}}{\beta_s}\sin\left(\frac{1}{2\sqrt{2}}\xi\beta_s z\right)\sin(\omega_{m-s} t - \beta_{m-s} z + \phi_m - \phi_s), \tag{A.17b}$$

$$v_{m+s}(z) = -\frac{V_0}{\sqrt{2}}\frac{\beta_{m+s}}{\beta_s}\sin\left(\frac{1}{2\sqrt{2}}\xi\beta_s z\right)\sin(\omega_{m+s} t - \beta_{m+s} z + \phi_m + \phi_s). \tag{A.17c}$$

One more comment is about the power relation. The average power associated with each signal is

$$P_s(z) = \frac{V_0^2}{2Z_0}\cos^2\left(\frac{1}{2\sqrt{2}}\xi\beta_s z\right), \tag{A.18a}$$

$$P_{m-s}(z) = \frac{V_0^2}{4Z_0}\left(\frac{\beta_{m-s}}{\beta_s}\right)^2\sin^2\left(\frac{1}{2\sqrt{2}}\xi\beta_s z\right), \tag{A.18b}$$

$$P_{m+s}(z) = \frac{V_0^2}{4Z_0}\left(\frac{\beta_{m+s}}{\beta_s}\right)^2\sin^2\left(\frac{1}{2\sqrt{2}}\xi\beta_s z\right), \tag{A.18c}$$

where $Z_0 = \sqrt{L'/C_0'}$ is the linear characteristic impedance of the transmission line. Given the input (A.15), we have

$$P_{in} = \frac{V_0^2}{2Z_0}. \tag{A.19}$$

The power change of the signal at the fundamental tone ω_s is $P_s - P_{in}$. It is now readily to see the Manley-Rowe relation [12] in the way of

$$\frac{P_s - P_{in}}{\beta_s} - \frac{P_{m-s}}{\beta_{m-s}} + \frac{P_{m+s}}{\beta_{m+s}} = 0. \tag{A.20}$$

References

[1] H. Bosma, "On stripline Y-circulation at UHF," *IEEE Trans. Microw. Theory Tech.*, vol. 12, no. 1, pp. 61–72, Jan. 1964.

[2] S. Tanaka, N. Shimomura, and K. Ohtake, "Active circulators – the realization of circulators using transistors," *Proc. IEEE*, vol. 53, no. 3, pp. 260–267, Mar. 1965.

[3] M. A. Smith, "GaAs monolithic implementation of active circulators," in *IEEE MTT-S Int. Microwave Symp. Dig.*, New York, NY, May 1988, pp. 1015–1016.

[4] S. Hara, T. Tokumitsu, and M. Aikawa, "Novel unilateral circuits for MMIC circulators," *IEEE Trans. Microw. Theory Tech.*, vol. 38, no. 10, pp. 1399–1406, Oct. 1990.

[5] S. Furukawa and S. Horiguchi, "The noise performance of the active circulator," *Proc. IEEE*, vol. 55, no. 11, pp. 2048–2050, Nov. 1967.

[6] A. Gasmi, B. Huyart, E. Bergeault, and L. Jallet, "Noise and power optimization of a MMIC quasi-circulator," *IEEE Trans. Microw. Theory Tech.*, vol. 45, no. 9, pp. 1572–1577, Sep. 1997.

[7] G. Carchon and B. Nauwelaers, "Power and noise limitations of active circulators," *IEEE Trans. Microw. Theory Tech.*, vol. 48, no. 2, pp. 316–319, Feb. 2000.

[8] C. H. Cox and E. I. Ackerman, "Photonics for phased array systems," in *Proc. IEEE Int. Symp. on Phased Array Systems and Technology*, Waltham, MA, Oct. 2010, pp. 607–610.

[9] ——, "Transmit isolating photonic receive links: a new capability for antenna remoting," in *Proc. Conf. Opt. Fiber Commun.*, Los Angeles, CA, Mar. 2011.

[10] ——, "Photonics for simultaneous transmit and receive," in *IEEE MTT-S Int. Microwave Symp. Dig.*, Baltimore, MD, Jun. 2011.

[11] A. V. der Ziel, "On the mixing properties of nonlinear condensers," *J. Appl. Phys.*, vol. 19, no. 11, pp. 999–1006, Nov. 1948.

[12] J. M. Manley and H. E. Rowe, "Some general properties of nonlinear elements – Part I. General energy relations," *Proc. IRE*, vol. 44, no. 7, pp. 904–913, Jul. 1956.

[13] H. E. Rowe, "Some general properties of nonlinear elements – Part II. Small signal theory," *Proc. IRE*, vol. 46, no. 5, pp. 850–860, May 1958.

[14] A. Suarez and R. Melville, "Simulation-assisted design and analysis of varactor-based frequency multipliers and dividers," *IEEE Trans. Microw. Theory Tech.*, vol. 54, no. 3, pp. 1166–1179, Mar. 2006.

[15] S. Magierowski, J.-F. Bousquet, Z. Zhao, and T. Zourntos, "RF CMOS parametric downconverters," *IEEE Trans. Microw. Theory Tech.*, vol. 58, no. 3, pp. 518–528, Mar. 2010.

[16] B. Gray, B. Melville, and J. S. Kenney, "Analytical modeling of microwave parametric upconverters," *IEEE Trans. Microw. Theory Tech.*, vol. 58, no. 8, pp. 2118–2124, Aug. 2010.

[17] Y. E. Wang, "Non-reciprocity with time-varying transmission lines (TVTLs)," in *IEEE Int. Conf. on Wireless and Information Technology Systems*, Maui, HI, Nov. 2012.

[18] P. K. Tien and H. Suhl, "A traveling-wave ferromagnetic amplifier," *Proc. IEEE*, vol. 46, no. 4, pp. 700–706, Apr. 1958.

[19] P. K. Tien, "Parametric amplification and frequency mixing in propagating circuits," *J. Appl. Phys.*, vol. 29, no. 9, pp. 1347–1357, Sep. 1958.

[20] S. Qin and Y. E. Wang, "Parametric conversion with distributedly modulated capacitors (DMC) for low-noise and non-reciprocal RF front-ends," in *IEEE MTT-S Int. Microwave Symp. Dig.*, Seattle, WA, Jun. 2013, accpeted and to be published.

[21] MA46580-1209 – M/A-COM Technology Solutions. [Online]. Available: http://www.macomtech.com/datasheets/MA46580_MA46585.pdf

[22] D. M. Pozar, *Microwave Engineering*, 3rd ed. New York, NY: Wiley, 2005.

[23] (2011) Data Sheet RO4000® Series – Rogers Corporation. [Online]. Available: http://www.rogerscorp.com/documents/726/acm/RO4000-Laminates—Data-sheet.pdf

[24] (2012) BAL-0006 – Marki Microwave. [Online]. Available: http://www.markimicrowave.com/assets/datasheets/BAL-0006.pdf

[25] W. Lee and E. Afshari, "Low-noise parametric resonant amplifier," *IEEE Trans. Circuits Syst. I, Reg. Papers*, vol. 58, no. 3, pp. 479–492, Mar. 2011.

[26] ——, "A CMOS noise-squeezing amplifier," *IEEE Trans. Microw. Theory Tech.*, vol. 60, no. 2, pp. 329–339, Feb. 2012.